

# The role of short and long range surface plasmons for plasmonic focusing applications

Avner Yanai and Uriel Levy

*Department of Applied Physics, The Benin School of Engineering and Computer Science, The Hebrew University of Jerusalem, Jerusalem, 91904, Israel*

[ulevy@cc.huji.ac.il](mailto:ulevy@cc.huji.ac.il)

**Abstract:** We propose and analyze a new plasmonic lens allowing the simultaneous focusing of both short and long range surface plasmons polaritons. The considered geometry is circularly symmetric and the SPP excitation is radially polarized. The long range and the short range modes are compared and found to have very different focusing properties. The trade-offs between the modes are discussed. The interplay between these two modes is used to demonstrate a practical focusing scenario providing a smaller spot size compared with previous version of plasmonic lenses, and a large depth of focus simultaneously.

© 2009 Optical Society of America

**OCIS codes:** (250.5403) Plasmonics; (240.6680) Surface plasmons; (310.2790) Guided waves.

---

## References and links

1. Z. W. Liu, J. M. Steele, W. Srituravanich, Y. Pikus, C. Sun, and X. Zhang, "Focusing surface plasmons with a plasmonic lens," *Nano Lett.* **5**, 1726-1729 (2005).
2. W. Srituravanich, L. Pan, Y. Wang, C. Sun, C. Bogy, and X. Zhang, "Flying plasmonic lens in the near field for high-speed nanolithography," *Nature Nanotech.* **3**, 733 - 737 (2008).
3. Q. Zhan, "Evanescent Bessel beam generation via surface plasmon resonance excitation by a radially polarized beam," *Opt. Lett.* **31**, 1726-1728 (2006).
4. A. Yanai and U. Levy, "Plasmonic focusing with a coaxial structure illuminated by radially polarized light," *Opt. Express* **17**, 924-932 (2009).
5. W. Chen and Q. Zhan, "Realization of an evanescent Bessel beam via surface plasmon interference excited by a radially polarized beam," *Opt. Lett.* **34**, 722-724 (2009).
6. G. Lerman, A. Yanai and U. Levy, "Demonstration of nano focusing by the use of plasmonic lens illuminated with radially polarized light," *Nano Lett.* **9**, 2139-2143 (2009).
7. S. A. Maier, *Plasmonics: Fundamentals and Applications* (Springer, New York, 2007).
8. D. Sarid, "Long-range surface-plasma waves on very thin metal films," *Phys. Rev. Lett.* **47**, 1927-1930 (1981).
9. P. Berini, "Plasmon-polariton waves guided by thin lossy metal films of finite width: bound modes of symmetric structures," *Phys. Rev. B* **61**, 10484-10503 (2000).
10. R. Charbonneau, N. Lahoud, G. Mattiussi, and P. Berini, "Demonstration of integrated optics elements based on long-ranging surface plasmon polaritons," *Opt. Express* **13**, 977-984 (2005).
11. A. Degiron and D. Smith, "Numerical simulations of long-range plasmons," *Opt. Express* **14**, 1611-1625 (2006).
12. K. Leosson, T. Nikolajsen, A. Boltasseva, and S. I. Bozhevolnyi, "Long-range surface plasmon polariton nanowire waveguides for device applications," *Opt. Express* **14**, 314-319 (2006).
13. M. I. Stockman, "Nanofocusing of optical energy in tapered plasmonic waveguides," *Phys. Rev. Lett.* **93**, 137404 (2004).
14. D. K. Gramotnev and K. C. Vernon, "Adiabatic nano-focusing of plasmons by sharp metallic wedges," *Appl. Phys. B Lasers Opt.* **86**, 7-17 (2007).
15. D. Gramotnev, M. Vogel, and M. Stockman, "Optimized nonadiabatic nanofocusing of plasmons by tapered metal rods," *J. Appl. Phys.* **104**, 034311 (2008).

16. E. Moreno, S. G. Rodrigo, S. I. Bozhevolnyi, L. Martin-Moreno, and F. J. Garcia-Vidal, "Guiding and focusing of electromagnetic fields with wedge plasmon-polaritons," *Phys. Rev. Lett.* **100**, 023901-1-4 (2008).
17. K. Kurihara, K. Yamamoto, J. Takahara and A. Otomo, "Superfocusing modes of surface plasmon polaritons in a wedge-shaped geometry obtained by quasi-separation of variables," *J. Phys. A Math. Theor.* **41** 295401 (2008).
18. E. Verhagen, A. Polman, and L. Kuipers, "Nanofocusing in laterally tapered plasmonic waveguides," *Opt. Express* **16**, 45-57 (2008).
19. L. Feng, D. Van Orden, M. Abashin, Q. Wang, Y. Chen, V. Lomakin, and Y. Fainman, "Nanoscale optical field localization by resonantly focused plasmons," *Opt. Express* **17**, 4824-4832 (2009).
20. A. Farjadpour, D. Roundy, A. Rodriguez, M. Ibanescu, P. Bermel, J. D. Joannopoulos, S. G. Johnson, and G. W. Burr, "Improving accuracy by subpixel smoothing in the finite-difference time domain," *Opt. Lett.* **31**, 2972-2974 (2006).
21. <http://ab-initio.mit.edu/meep/>

## 1. Introduction

Focusing of surface plasmon polaritons (SPPs) by plasmonic lenses (PLs) was shown to be useful in confining electromagnetic fields at the sub-wavelength scale [1, 2]. The combination of short SPP wavelength and planar focusing allows the realization of such lenses with effective numerical aperture (NA) larger than the refractive index of the surrounding dielectric material. The SPP wave is TM polarized and thus it becomes clear that the incident polarization plays a significant role, affecting the PL's functionality. It was proposed [3, 4] and demonstrated [5, 6] that by illuminating the PL with radially polarized a stronger, tighter and circularly symmetric spot is obtained at the focus, compared with linear polarization illumination. It was also shown that the focusing efficiency could be enhanced by integrating Bragg reflectors and grating couplers into the device [4].

The spot size obtained by PLs is limited by the SPP wavelength. Although the SPP wavelength is inherently smaller than that of a free space mode with the same frequency, the difference is typically small for thick metals in the visible and the infrared regime. However, modification of the SPP wavelength is possible by changing the thickness of the metallic layer of the PL. We therefore wish to explore the effects of the metal thickness on the PL's focusing characteristics. The paper is structured as follows. In section 2 the profile of the standing wave SPPs along a PL that comprises of a circular disk are described. In section 3, we study the figure of merits of the PL for the long range and the short range modes independently. In section 4, we consider a specific PL geometry and investigate numerically (using finite-difference time-domain, (FDTD) calculations) its focusing characteristics. We show that the spot size can be reduced compared with previous PL's versions.

Throughout the paper we consider circular symmetric PL structures and radial polarization illumination which was shown to provide advantages both in efficiency and in spot size. Thus, our problem in hand does not vary with the azimuthal angle  $\theta$ .

## 2. SPP field distribution on a metallic circular disk

First, we express the SPP field components, resident on the surface of a metallic circular disk. The SPPs are excited by radially polarized light, and their propagation vector ( $\beta$ ) is directed along the radial direction. The structure is depicted in Fig. 1. The decay constants into the metal and the dielectric are designated by  $k_i$  where  $i=M,D$  stands for the metallic and dielectric regions respectively.

For our purposes, the relevant subset of Maxwell's curl equations in cylindrical coordinates is:

$$\frac{\partial E_r}{\partial z} - \frac{\partial E_z}{\partial r} = -j\omega\mu H_\theta \quad (1)$$

$$\frac{1}{r} \frac{\partial H_z}{\partial \theta} - \frac{\partial H_\theta}{\partial z} = j\omega \epsilon_0 \epsilon_i E_r \quad (2)$$

$$\frac{1}{r} H_\theta + \frac{\partial H_\theta}{\partial r} - \frac{1}{r} \frac{\partial H_r}{\partial \theta} = j\omega \epsilon_0 \epsilon_i E_z \quad (3)$$

The SPP is a TM mode, resulting:

$$H_r = E_\theta = H_z = 0 \quad (4)$$

Assuming a bound SPP mode and no angular dependency (both the structure and the illumination have no angular variance) gives the following relations at  $z \geq 0$ :

$$\frac{\partial}{\partial z} = -k_D, \quad \frac{\partial}{\partial r} = j\beta, \quad \frac{\partial}{\partial \theta} = 0, \quad k_D^2 = \beta^2 - \omega^2 \epsilon_0 \epsilon_D \mu \quad (5)$$

Substituting Eq. (4) in Eqs. (2) and (3) results in:

$$-\frac{\partial H_\theta}{\partial z} = j\omega \epsilon_0 \epsilon_i E_r \quad (6)$$

$$\frac{1}{r} H_\theta + \frac{\partial H_\theta}{\partial r} = j\omega \epsilon_0 \epsilon_i E_z \quad (7)$$

The substitution of Eq. (1) in (7) gives:

$$\frac{1}{r} \left[ \frac{\partial E_r}{\partial z} - \frac{\partial E_z}{\partial r} \right] + \frac{\partial \left[ \frac{\partial E_r}{\partial z} - \frac{\partial E_z}{\partial r} \right]}{\partial r} = -\omega^2 \mu \epsilon_0 \epsilon_i E_z \quad (8)$$

By eliminating  $E_r$  from Eq. (8) with Eqs. (6) and (7) and then utilizing Eq. (5) we obtain:

$$\frac{\partial^2 E_z}{\partial r^2} + \frac{1}{r} \frac{\partial E_z}{\partial r} + \beta^2 E_z = 0 \quad (9)$$

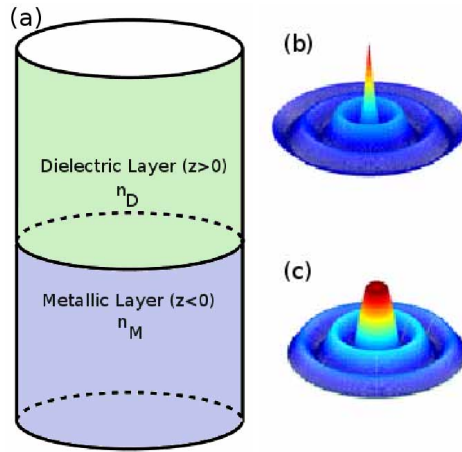


Fig. 1. Schematics of the cylindrical metallic disk and its resulting intensity patterns: (a) structure geometry. (b) Schematic pattern of  $|E_z|^2$  corresponding to Eq. (11). (c) Schematic pattern of  $|E_r|^2$  corresponding to Eq. (12)

$$E_r = -j \frac{k_D}{\beta^2} \frac{\partial E_z}{\partial r} \quad (10)$$

The solution for Eqs. (9) and (10) is given by:

$$E_z(r, z) = A J_0(\beta r) \exp(-k_D z) \quad (11)$$

$$E_r(r, z) = -A j \frac{k_D}{\beta} J_1(\beta r) \exp(-k_D z) \quad (12)$$

Eqs. (11) and (12) describe the electric field distribution that is bounded to the disk surface at the upper half plane ( $z \geq 0$ ). Similar expressions can be written for the lower half plane ( $z \leq 0$ ) by replacing  $k_D$  with  $k_M$  with the appropriate sign resulting in:

$$E_z(r, z) = B J_0(\beta r) \exp(k_M z) \quad (13)$$

$$E_r(r, z) = B j \frac{k_M}{\beta} J_1(\beta r) \exp(k_M z) \quad (14)$$

Where A and B are arbitrary amplitude constants. From continuity of  $E_r$  and  $\epsilon_i E_{z,i}$  at  $z=0$  one readily obtains that  $k_D/k_M = -\epsilon_D/\epsilon_M$  which is the same relation that holds for the standard 1D bi-layered plasmonic waveguide in Cartesian coordinates resulting in the well known characteristic equation  $\beta = k_0 \sqrt{\frac{\epsilon_M \epsilon_D}{\epsilon_M + \epsilon_D}}$ . Following the same procedure, it can be shown that the SPP characteristic equation of a multilayered disk (layered along the Z-direction) is the same as its 1D multilayered Cartesian equivalent.

As a final remark, we note the resemblance of the above derivation and Eqs. (11) and (12) to the  $TM_{01}$  mode of a circular metallic waveguide propagating in the z direction.

### 3. Focusing characteristics for long and short range SPPs for a circular disk

When considering a symmetric insulator/metal/insulator (IMI) multilayer structure [7] two bounded modes can be excited, with symmetric and antisymmetric profiles of the electric field component along the propagation direction (i.e.  $E_r$ ) [8, 9, 10, 11, 12]. The antisymmetric mode (or odd mode) is less confined compared with the symmetric (even) mode. It has a larger SPP wavelength and evolves it into the TEM mode of the surrounding dielectric as the metallic layer thickness decreases [9]. The symmetric mode shows the opposite trend: it gets more confined within the metal as the metal layer thickness decreases. This results in a shorter SPP wavelength, a shorter decay length into the surrounding dielectric, and a smaller propagation distance, due to enhancement of ohmic losses. Because of that, the antisymmetric mode is often termed a long range SPP (LRSPP) and the symmetric mode a short range SPP (SRSPP).

In this section, we will consider the focusing characteristics of both SPP modes for an IMI disk, layered along the Z-direction. Following the discussion in section 2, the characteristic equation of such disk is the same as that of the 1D IMI equivalent, which can be split into two equations, describing the LRSPP and SRSPP modes propagating along an IMI structure with metal thickness h (see ref. [7]):

$$\tanh\left(\frac{1}{2} k_M h\right) = -\frac{k_D \epsilon_M}{k_M \epsilon_D} \quad (15)$$

$$\tanh\left(\frac{1}{2} k_M h\right) = -\frac{k_M \epsilon_D}{k_D \epsilon_M} \quad (16)$$

Throughout this section, we will present analytic results that are calculated on the basis of Eqs. (11) - (16).

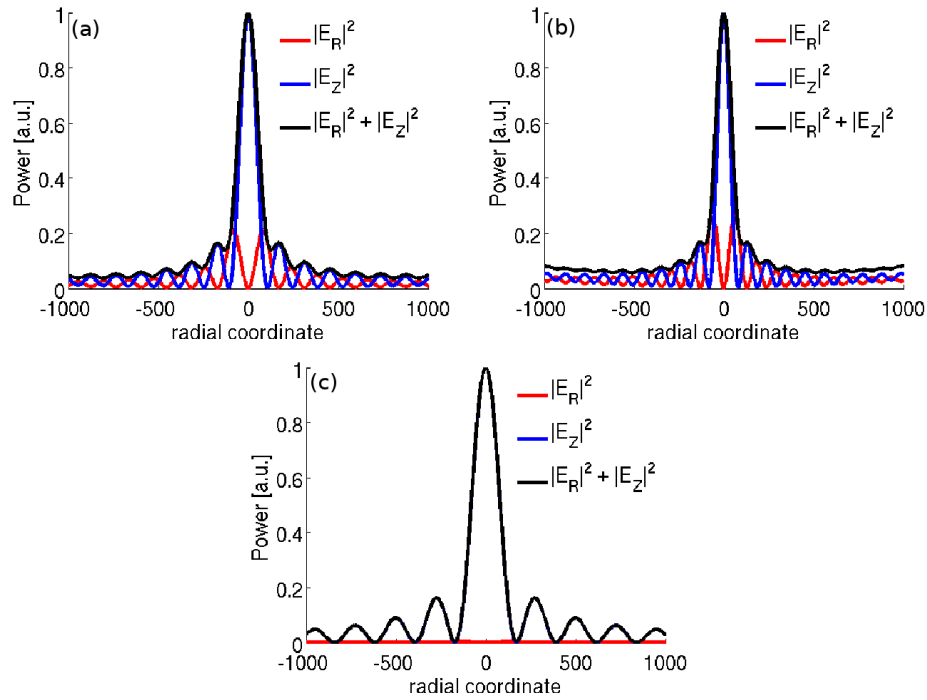


Fig. 2. SPP lateral field intensity distribution on the surface of the thin metallic disk embedded in a dielectric with  $n=1.33$ . The fields are calculated in the air. (a) SRSPP mode with metallic layer thickness  $h=15$  nm. (b) SRSPP mode,  $h=10$  nm. (c) LRSPP mode,  $h=15$  nm.

Fig. 2 shows the electrical energy density components obtained by the excitation of a thin layer of silver ( $\epsilon_M = -13.9 + 0.65i$ ) embedded in a dielectric environment with refractive index  $n=1.33$  (this environment will be later used in section 4). The excitation wavelength is  $\lambda_0 = 600$  nm. Fig. 2(a) and 2(b) show the results of the SRSPP mode for layer thickness of 15 and 10 nm respectively. A smaller central lobe is obtained for the 10 nm thick layer, indicating a shorter SPP wavelength. In addition, the contribution of the radial field becomes more significant as the layer thickness decreases (this will be further discussed in section 3.2). From Fig. 2(b), one can notice that at the edges of the PL the energy density decreases towards the middle of the structure. This is because of the very significant propagation losses for a 10 nm thick layer. A turning point is obtained around  $r=500$  nm, where the focusing overcomes this loss. Finally, Fig. 2(c) shows the result of a LRSPP mode for layer thickness of 15 nm. The  $E_r$  component is seen to be negligible, indicating that the SPP wavelength of this mode is very similar to the vacuum wavelength. Further decrease of the layer has a negligible effect on the LRSPP mode.

### 3.1. Figures of merit

To evaluate the performance of the PL, we consider four figures of merit (FOM). The first two are the spot size (SPSZ) and the depth of focus (DOF), previously defined for a plasmonic lens in [4] as the FWHM of the electric energy density along the radial direction and the distance along the  $z$  direction for which the electric energy density drops by a factor of two, respectively. The other two FOMs are the effective numerical aperture defined as  $NA_{\text{eff}} = \lambda_0 / (\lambda_{\text{SPP}} \times n_D)$  (this criterion represents the improvement factor of the PL's NA compared to that of a dielectric lens with a nearly zero focal length, i.e. having the highest possible NA for a given  $n_D$ ) and

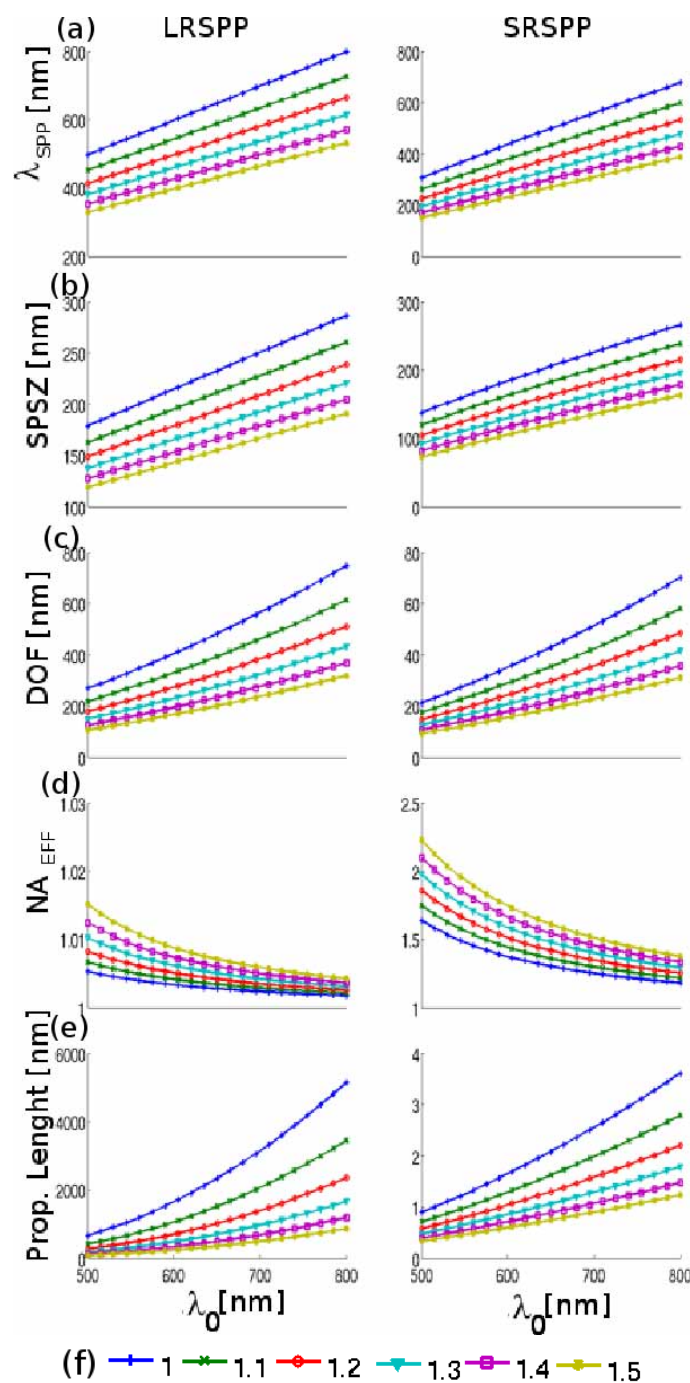


Fig. 3. FOMs of the PL. The left and the right columns correspond to LRSP and SRSP excitations respectively. (a)-(e)  $\lambda_{SPP}$ , SPSZ, DOF,  $NA_{eff}$  and the propagation length respectively, as a function of the excitation wavelength  $\lambda_0$ . (f) Legend for (a)-(e) specifying the refractive index  $n_D$  surrounding the metal.

the propagation length  $L = 1/(2 \times \text{Im}[\beta])$ . Fig. 3 presents these FOMs versus the excitation wavelength for a circular silver disk with metal thickness  $h=15$  nm embedded in a dielectric medium. We vary the refractive index of the dielectric between  $n_D = 1$  and  $n_D = 1.5$ . The results show the trade-off between the FOMs obtained by the LRSPP and the SRSPP modes. The SRSPP mode possesses a smaller SPP wavelength and therefore a smaller SPSZ at the cost of a smaller DOF due to tighter confinement to the interface. The LRSPP however, exhibits the opposite behavior. The effective NA provides an interesting comparison between the PL and a standard dielectric lens. Since the LRSPP evolves into the TEM mode of the surrounding dielectric as the metallic layer thickness decreases [9],  $NA_{\text{eff}}$  approaches the value of unity. For the SRSPP mode however,  $NA_{\text{eff}}$  grows significantly as the dielectric index or the optical frequency increase because of its highly dispersive nature. Unfortunately, the improvement in NA is coupled to higher loss. Nevertheless, an improvement factor of  $\approx 1.5$  is achievable with moderate loss.

To summarize, the two modes offer two distinct and possibly useful focusing characteristics: The SRSPP provides a very high numerical aperture lens, but with fast decaying energy, both in the  $z$  and in the propagation direction ( $r$ ). The LRSPP, because of its large DOF (that can be of the order of the free space optical wavelength) provides a slowly decaying “light bullet” in the  $z$  direction. Unfortunately, the improvement in the resulting NA is smaller in this case. A

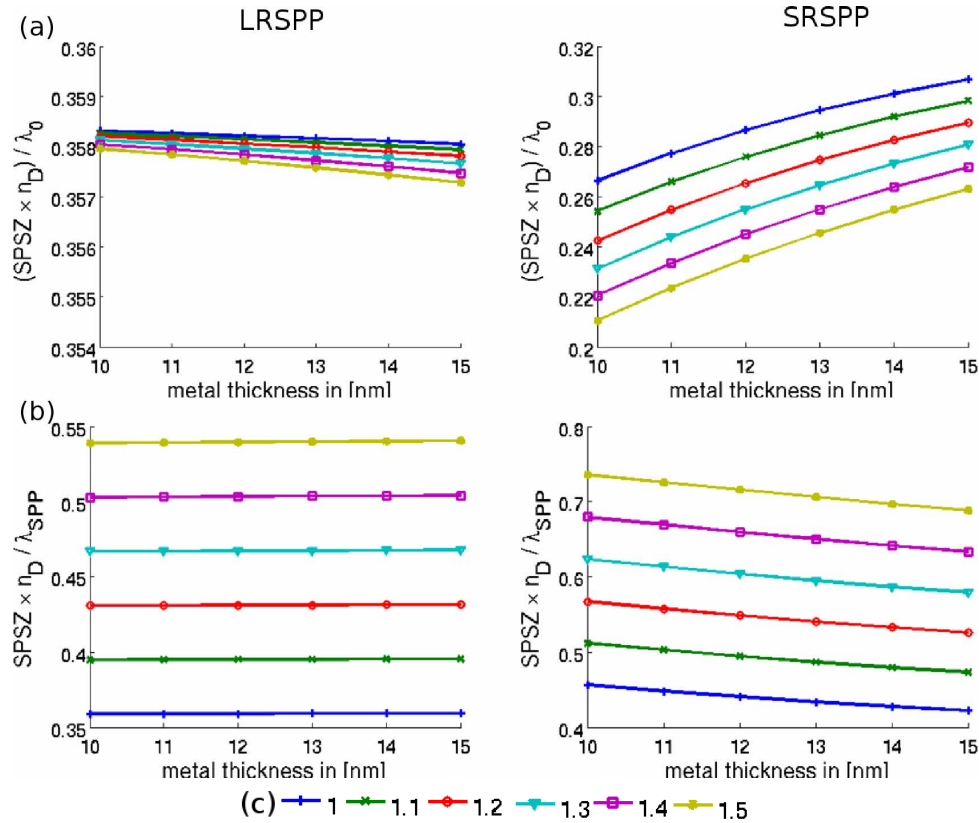


Fig. 4. (a) SPSZ Normalized by  $(\lambda_0/n_D)$  as a function of the metal thickness. (b) SPSZ Normalized by  $(\lambda_{SPP}/n_D)$  as a function of the metal thickness. (c) Legend for (a)-(b) specifying the refractive index  $n_D$  surrounding the metal.



combination of the two modes may become useful, as discussed in section 4.

### 3.2. Longitudinal and transverse electric components, and their effect on the spot size

As previously stated in [4, 6], the advantage of using radially polarized light over linearly polarized light relies on the fact that in the dielectric region, the out of plane SPP electric field component (i.e. the field along the  $z$  direction) is inherently larger than the in plane electric field component. This is because for a 1D plasmonic structure  $|E_z|^2/|E_r|^2 = |k_r|^2/|k_z|^2$  and  $|k_r|^2 > |k_z|^2$  is a necessary condition to support a bound mode. Under radial polarization illumination the out of plane field interferes constructively at the center (see Eq. (11)) resulting in a smaller spot size compared to that obtained by linear polarization illumination [1]. Unfortunately, as can be seen from Eq. (12) and Fig. 2, the in plane ( $E_r$ ) field broadens the spot size although it has no contribution to the total electric field density ( $|E_z|^2 + |E_r|^2$ ) at  $r=0$ . For a metallic layer thickness well above the metal skin depth the SPPs at each side are uncoupled and one can assume that the SPP dispersion relation is similar to the dispersion of an interface between semi-infinite metal and dielectric layers. For such a case  $|E_z|^2/|E_r|^2 = |k_r|^2/|k_z|^2 = |\epsilon_M|/\epsilon_D > 1$ . However, as the metal thickness is decreased, the SRSP evolves to reside more in the metal and the ratio  $|E_z|^2/|E_r|^2 = |k_r|^2/|k_z|^2$  decreases towards unity. Therefore, we anticipate two opposite trends: while the ratio  $\text{SPSZ}/\lambda_0$  decreases with the decrease of the metal thickness (because  $\lambda_{\text{SPP}}$  decreases), the ratio  $\text{SPSZ}/\lambda_{\text{SPP}}$  increases, because of the more significant contribution of the undesired  $E_r$  component. In contrast, the LRSP exhibits a nearly flat  $\text{SPSZ}/\lambda_{\text{SPP}}$  ratio. This is because for this mode  $|E_r|$  is negligible. These trends can be observed in Fig. 4, calculated for  $\lambda_0=600$  nm.

## 4. Numerical analysis of a focusing scheme

In this section we propose a circular wedge configuration for realizing a PL that exhibits a combination of LRSP and SRSP. Fig. 5 shows the cross-section and 3-D view of the proposed structure. As can be seen, the structure combines a central section made of a plain circular metallic layer with radius  $f$  and thickness  $h$ , surrounded by an outer wedge-like circular section with initial thickness  $w$ . The overall radius of the structure is  $d$ . The focusing is obtained at the center of the structure ( $r=0$ ). Wedge-like and adiabatic structures attract much interest in plasmonic research, primarily for confinement of electromagnetic waves [13, 14, 15, 16, 17, 18, 19]. Here we use the wedge-like structure for adiabatic shrinkage of the metallic layer

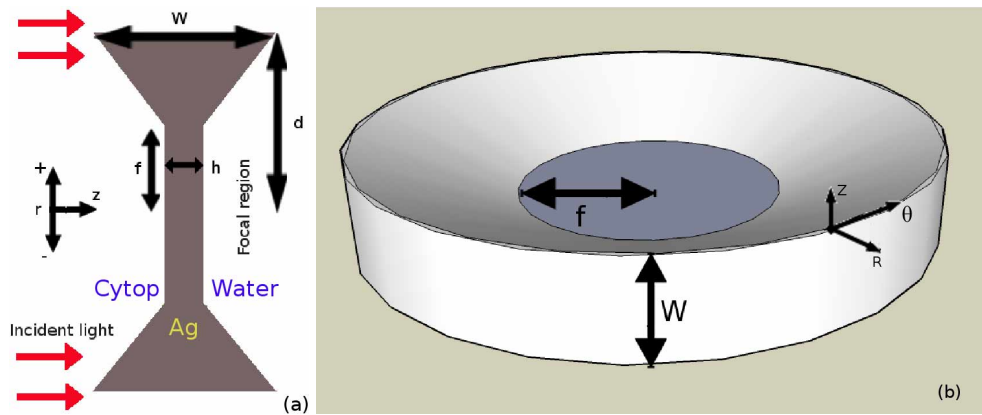


Fig. 5. (a) Schematic diagram of the cross-section of the circular wedge (b) 3-D view of the circular wedge



thickness, and because the wide edges and their sharp corners are suitable for excitation of SPPs. The adiabatic structure is important to obtain the thin metallic layer needed, with as small as possible back-reflections due to mode mismatch. The wedge is placed on top of a Cytop layer. To cope with bio-imaging applications, the focal region is embedded in water based liquid. Both Cytop and the water based liquid have a refractive index  $n \approx 1.33$ , ensuring the symmetry needed for LRSPP and SRSPP.

Fig. 6 shows the focusing of the two distinct modes, as calculated by FDTD. For our calculations we use Meep [20], a free-software FDTD package available at [21]. First, we investigate the structure by the excitation of pure symmetric and anti-symmetric modes. These modes are excited by sources with the corresponding symmetry. The excitation vacuum wavelength is  $\lambda_0 = 600$  nm. The geometrical parameters are  $w=70$  nm,  $d=4200$  nm,  $f=2100$  nm, and  $h=15$  nm and computational cell resolution of 2 nm. Fig. 6 shows the resulting electric energy density patterns for both pure modes. It is apparent that in Fig. 6(a) that the energy density comprises of two contributions: 1 - contribution from the SRSPP mode that is bounded to the surface and 2 - contribution due to diffraction of light from the edges of the sample. Diffraction exists also in Fig. 6(b), but is less apparent because of the existence of the slowly decaying LRSPP mode.

Next we consider a practical scenario of illuminating the structure by radially polarized light having a Bessel like field distribution. For numerical reasons, the incident light is modeled as a truncated radially polarized Bessel beam with field distribution  $E_r = J_1(\alpha r) \times U(r - r_0)$ , where  $\alpha$  is a scaling factor,  $r$  is the radial coordinate  $U(r)$  is the step function ( $U(r)=1$  for  $r \geq 0$ ,  $U(r)=0$  for  $r < 0$ ) shifted by  $r_0$ . This incident field is an approximation to the donut shaped radially polarized mode. This donut shape is favorable as it avoids light from incident at the thin metal section. Such light would partially penetrate through the thin metal resulting in the broadening of the focused spot.

In Fig. 7(a) one can see an FDTD calculation showing the electric energy density resulting from an illumination function having the following parameters:  $\lambda_0 = 600$  nm,  $\alpha = 0.1 [\mu\text{m}^{-1}]$ , and  $r_0 = 200$  nm. The geometrical parameters are the same as those used for Fig. 6. The thin wedge is better observed in Fig. 7(b) which provides a zoom near the focal region.

In a practical illumination scenario (as the one described above), the two modes (symmetric and anti-symmetric) are excited simultaneously. In order to evaluate the symmetry of the field at the focus, we define a function that measures the excited mode parity. The function com-

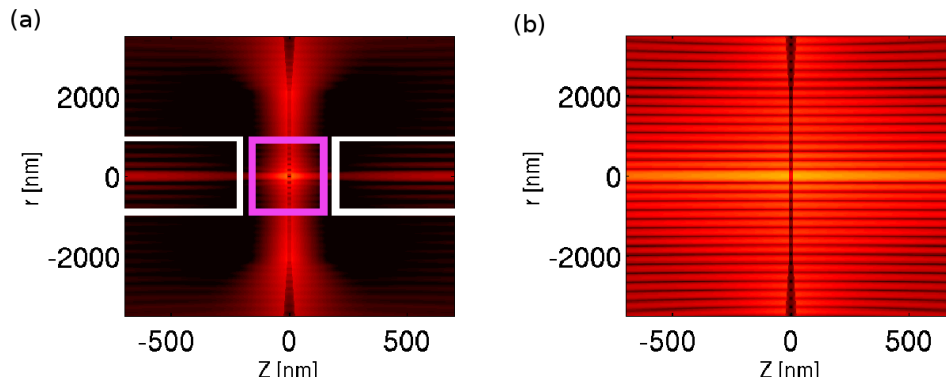


Fig. 6. FDTD simulation showing the total electric energy density (logarithmic color scaling) for: (a) excitation of a pure symmetric mode. The region designated by the purple rectangle is dominated by the energy density of the SRSPP. The region designated by the white rectangle is dominated by energy density originated from diffraction and radiation from the wedge. (b) excitation of a pure anti-symmetric mode

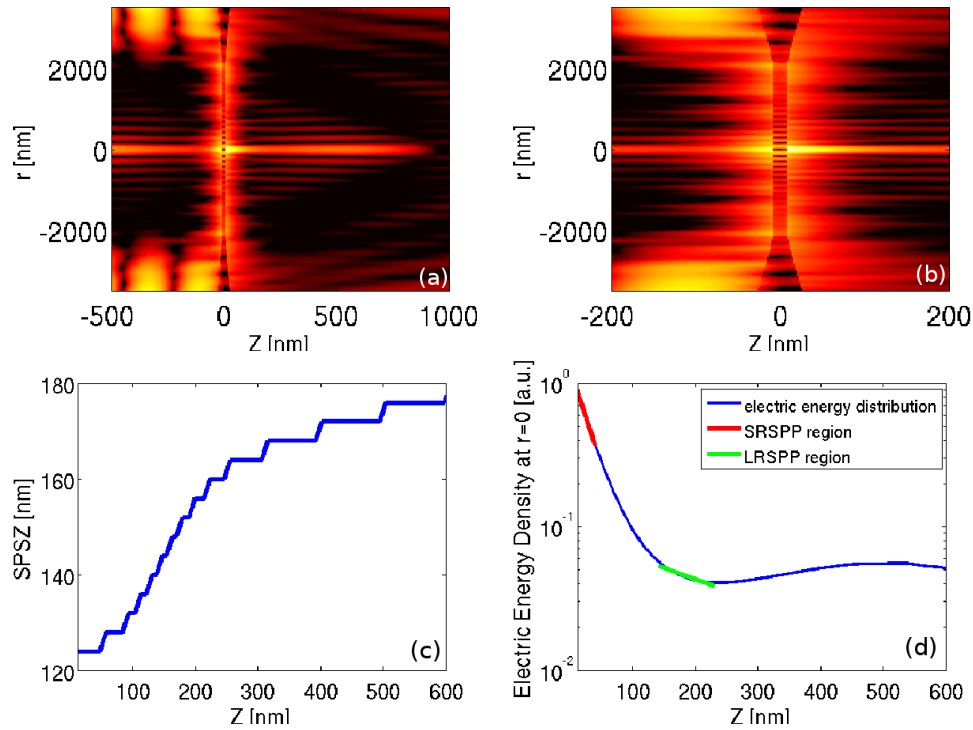


Fig. 7. (a) Electric energy density (logarithmic color scaling) resulted by excitation of LR-SPP and SRSP modes using radially polarized light illumination. (b) Zoom of Fig. 7(a) in the vicinity of the focal region (c) The resulting SPSZ as a function of the distance (along the  $z$  axis) from the center of the metallic layer. (d) The normalized electric energy density at the center as a function of the distance from the metallic surface.

compares the sign of the SPP magnetic component ( $H_\phi$ ) at two points on both sides of the metallic layer ( $z=\pm h/2$ ,  $r=0$ ) at each time step of the FDTD solver, and accumulates the sign comparisons over a single time period of the optical frequency. At each time step, in case the sign is equal, the function adds -1 to the accumulation. Otherwise, it adds +1. This can be formulated as:  $S = (\Delta t/T) \sum_{n=1}^{T/\Delta t} \text{Neq}[\text{sgn}(H_\phi(P_1)), \text{sgn}(H_\phi(P_2))]$  where “ $S$ ” is the symmetry measurement function,  $\Delta t$  is the time interval of the FDTD solver,  $T$  is the time period, “ $\text{Neq}[x,y]$ ” is a function that returns -1 if  $x=y$  and +1 otherwise, and “ $\text{sgn}$ ” is the sign function.  $P_1$  and  $P_2$  are two measurement points at  $r=0$  and  $z=\pm h/2$ . The normalization factor  $\Delta t/T$  ensures that  $S$  returns a value in the range  $[-1,+1]$ , where the cases  $S=-1$  and  $S=+1$  correspond to pure anti-symmetric and symmetric modes respectively.

The symmetry function returned a value of 0.697 indicating that mostly SRSP are excited. Indeed, it can be observed in Fig. 7(c) that the SPSZ in the vicinity of the surface is 124 nm, which is close to the analytically expected value for the SRSP mode (125.5 nm). Around  $z=220$  nm the SPSZ reaches the value of 160 nm, whereas 162 nm is the analytically expected value of the SPSZ due to LRSP. The SPSZ continues to grow with  $Z$ . This can be explained by the contribution of free space modes originating from diffraction and radiation from the wedge. The 4 nm discontinuities in Fig. 7(c) are due to the 2 nm resolution used in the FDTD calculation.

A different approach to try to understand the contribution of the various modes along the  $Z$ -

axis, is by looking at the normalized electric energy at the center as a function of  $Z$  (Fig. 7(d)). A linear fit is able to reveal the SPP decay constants (mind the semi-logarithmic scale). In Fig. 7(d), the red line shows the linear fit performed near the surface, indicating a decay constant of 0.031 [1/nm], whereas the analytic value for the energy decay factor of the SRSPP mode is 0.035 [1/nm]. The region where the SRSPP have decayed enough and therefore is dominated by LRSPP, is harder to localize because the contribution of non-SPP waves originating from diffraction and radiation grows with  $Z$ . However, at  $Z=200$  nm the fit (green line) that indicated a decay constant of 0.0036 [1/nm], (analytic expected value for the LRSPP is 0.0032 [1/nm]). We also note that in this region the SPSZ is identical to the theoretical expected value resulting from LRSPP excitation. The increase in energy density that is observed at higher  $Z$ -values is attributed to diffraction and radiation from the edges of the sample. Further investigation is needed, in order to understand the contribution of the various modes more thoroughly.

## 5. Conclusions

We propose and investigate a novel wedge-like plasmonic lens (PL) configuration for focusing of short range and long range surface plasmons. The considered geometry is circularly symmetric and the SPP excitation is radially polarized. The long range and the short range modes are compared and found to be very different in their focusing properties. The trade offs between using these modes for focusing is discussed. We take advantage of the interplay between these two modes to demonstrate a practical focusing configuration providing smaller spot size compare with previous versions of PLs, and large depth of focus simultaneously. Specifically, the SRSPP has its energy tightly bounded to the metal surface with a spot size as small as 125.5 nm for  $\lambda_0=600$  nm (equivalent to a  $NA_{\text{eff}}$  of 1.61), and the LRSPP exhibits a slowly decaying field but with a larger spot size of 162 nm. Such a device may become useful for microscopy, nano-lithography, sensing and bio-sensing applications.

## Acknowledgments

The authors are grateful to Mark I. Stockman for fruitful discussions and would like to acknowledge the support of the Israeli Science Foundation, the Israeli Ministry of Science and the Peter Brojde Center for Innovative Engineering and Computer Science.